Integrated Simulation of ELM Energy Loss and Cycle in Improved H-mode Plasmas

N. Hayashi[1], T. Takizuka[1], N. Aiba[1], N. Oyama[1], T. Ozeki[1], S. Wiesen[2], V. Parail[3]

1) Japan Atomic Energy Agency, Naka, Ibaraki-ken, 311-0193 Japan
2) Euratom FZJ Association, Institute of Energy Research, IEF-4 52425 Julich, Germany
3) Euratom UKAEA Fusion Association, Culham Science Centre, Abingdon OX14 3DB UK

e-mail contact of main author: hayashi.nobuhiko@jaea.go.jp

Abstract. The energy loss due to an edge localized mode (ELM) crash and its cycle have been studied by using an integrated transport code with a stability code for peeling-ballooning modes and a transport model of scrape-off-layer (SOL) and divertor plasmas. The integrated code reproduces a series of ELMs with the following characteristics. The ELM energy loss increases with decreasing the collisionality and the ELM frequency increases linearly with the input power, as the same as experiments of type-I ELMs. A transport model with the pedestal neoclassical transport connected to the SOL parallel transport reproduces the inter-ELM transport, which decreases in the low collisionality so that the ELM loss power is enhanced as observed in experiments. The inter-ELM energy confinement time agrees with the scaling based on the JT-60U data. The steep pressure gradient inside the pedestal top, required for improved H-mode plasmas with the H_{H98y2} factor above unity, is found to enhance the ELM energy loss and reduce the ELM frequency so that the ELM loss power remains constant. The steep pressure gradient inside the pedestal top broadens the region of the ELM enhanced transport and induces subsequent instabilities. When the large energy is transported near to the separatrix by the instabilities, a subsequent instability arises near the separatrix and makes an additional loss.

1. Introduction

Edge localized modes (ELMs) induce sometimes very large heat load to divertor plates and cause the reduction of plate lifetime. The ELMs, however, are expected to sustain a H-mode plasma without the accumulation of impurities. The ELM cycle consists of two phases: an ELM crash by the MHD instability inducing the energy loss from the pedestal plasma and a quiescent phase recovering the pedestal energy between ELMs (inter-ELM phase). Analyses from multi-machine experiments showed that the ELM energy loss increases with decreasing the collisionality [1-3] and the inter-ELM transport increases with the collisionality [3,4]. Effects of the bootstrap current and the scrape-off-layer (SOL) transport on the ELM energy loss, and an effect of the neoclassical transport on the inter-ELM transport have been discussed in [1,2] and [4], respectively. The physical understanding and quantitative evaluation are, however, not fully accomplished so far.

The integrated simulation code is one of effective methods to study the ELM mechanism [5-9]. For example, an integrated code COCONUT, which integrates 1.5 dimensional (1.5D) core transport code JETTO and 2D divertor code EDGE2D, has been developed and is being used for the study of ELM dynamics [8]. On the other hand, we have developed an integrated code TOPICS-IB [9] with a dynamic five-point model for SOL-divertor plasmas [10] and a stability code for peeling-ballooning modes, MARG2D [11]. The TOPICS-IB is based on a 1.5D core transport code TOPICS extended to the integrated simulation for burning plasmas. The TOPICS-IB clarified the physical mechanism of the ELM energy loss, such as the collisionality dependence of the energy loss caused by the edge bootstrap current and the SOL transport [9,12,13]. In the previous study, however, only one ELM crash was examined. The ELM cycle following the first ELM has not yet been investigated.

In this paper, we study the ELM energy loss and cycle by using the TOPICS-IB. We examine

the relation between the ELM cycle and the energy loss influenced not only by the collisionality and but also by the steep pressure gradient inside the pedestal, which is required for improved H-mode plasmas with the H_{H98y2} factor above unity. The input-power dependence and the inter-ELM transport are investigated and compared with experiments.

2. Integrated code TOPICS-IB for the ELM dynamics

The ELM dynamics is investigated by the TOPICS-IB, in which the TOPICS is coupled with the ELM model [9], the SOL-divertor model [10] and neutral models [13]. Details of the TOPICS-IB are shown in [9,13]. Some essential features are explained as follows.

2.1. 1.5D transport code TOPICS

TOPICS self-consistently solves the 1D transport and current diffusion equations and the Grad-Shafranov equation of the MHD equilibrium on the 2D plane. The transport equations are the continuity equation for the deuterium ion density, n_i, the power balance equations for the electron temperature, T_e, and the ion temperature, T_i, on the coordinate of the normalized minor radius, ρ. In this paper, particle and thermal diffusivities are assumed as $D = D_{neo,i} + D_{ano}$ and $\chi_{e,i} = \chi_{neo,i} + \chi_{ano,e,i}$, where $D_{neo,i}$ and $\chi_{neo,i}$ denote neoclassical ion diffusivities. The anomalous diffusivities D_{ano} and $\chi_{ano,e,i}$ are simply given as an empirical formula based on JT-60U experiments, $D_{ano} = \chi_{ano,e} = 0.18 \ (1+2\rho^3) \ (1+P_{NB}^{0.5}) \ m^2/s$ and $\chi_{ano,i} = 2 \ \chi_{ano,e}$, where P_{NB} is the neutral beam power in the unit of MW. In order to produce the H-mode pedestal structure, the transport near the edge is reduced to the neoclassical level ($D_{ano} = \chi_{ano,e,i} = 0$). This pedestal transport model is supported by the experimental observation that the electron heat diffusivity between ELMs was reduced to the ion neoclassical level [4]. The pedestal width, Δ_{ped}, is prescribed for simplicity. The neutral transport in the core region is solved by the 2D Monte-Carlo method. The particle flux of neutrals across the separatrix derived from the particle balance model in subsection 2.4 is used as an input for the Monte-Carlo code.

2.2. ELM model

The ELM model [9] has been developed by coupling the TOPICS with a linear MHD stability code MARG2D [11]. In the present simulation, stabilities of $n = 1$-50 modes are examined at given time-intervals, where n is the toroidal mode number. When some modes become unstable, an ELM is assumed to occur. The ELM enhanced diffusivities, D_{ELM} and χ_{ELM}, are added on the basis of eigenfunction profiles of unstable modes, where $D_{ELM} = \chi_{ELM} = \chi_{ELM}^{max} \times (\Sigma_n \ \xi_{r,n}^2)/N$, where χ_{ELM}^{max} is the maximum value, $\xi_{r,n}$ denote the radial displacement of the plasma by the unstable mode with specific n, and N is the total number of the unstable modes with various n. The profile of the radial displacement $\xi_{r,n}$ is assumed to be the sum of poloidal mode components of the eigenfunction, $\xi_{r,n,m}$, i.e., $\xi_{r,n} \propto \Sigma_m \xi_{r,n,m}$, where $\xi_{r,n}$ is normalized by its maximum value. The ELM enhanced transport is maintained for a time interval τ_{ELM} given as a parameter.

2.3. SOL-divertor model

The five-point model [10] is based on the integral of time-dependent fluid equations, i.e., particle, momentum, electron and ion temperatures, generalized Ohm's law and current equations. The model geometry is an open magnetic flux-tube nearest to the separatrix. The flux tube is divided into four regions and the integral fluid equations in each region are reduced to a set of nonlinear equations with physical variables at five positions (stagnation

point, upstream throats of divertor regions and sheath entrances). Exponential radial profiles with e-folding lengths, λ_n, λ_{Te}, λ_{Ti}, are assumed. The five-point model can deal with the asymmetry of divertor plasmas, but the symmetry is assumed in this paper for simplicity. Electron particle flux and heat fluxes of electrons and ions across the separatrix, Γ_{re}, Q_{re}, Q_{ri}, obtained in the TOPICS are used as inputs for the five-point model. Heat and particle diffusivities in the five-point model, $D_\perp$, $\chi_{e\perp}$ and $\chi_{i\perp}$, are set equal to those values at the separatrix in the TOPICS. The five-point model calculates the SOL electron density at the separatrix, n_{eSOL}, and temperatures, T_{eSOL} and T_{iSOL}, which are used as boundary conditions in the TOPICS. The particle source density due to recycling neutrals in the divertor region, S_d, is given by $S_d = \eta'_r \Gamma_d / L_d$ where Γ_d and L_d denote a particle flux to the divertor plate and a length of the divertor region along the magnetic field line, respectively. The divertor recycling coefficient η'_r is modeled by $\eta'_r = (1 - f_{dpump} - f_{dr})(1 - \exp(-\theta L_d / (\upsilon_n / (n_{ediv} < \sigma\upsilon >_{iz}))))$ where θ is the pitch of the magnetic field and the neutral velocity $\upsilon_n = (T_n/m)^{0.5}$. The fraction f_{dpump} is pumped out from the divertor and the fraction f_{dr} radially escapes the divertor region and goes back to the core region. The ionization rate coefficient $<\sigma\upsilon>_{iz}$ is a strong function of the divertor electron temperature, T_{ediv}.

2.4. Integration of neutral models

We consider the particle balance in the whole regions and integrate neutral models in the TOPICS and the five-point model [13]. Plasma particle flow across the separatrix, Φ_r, goes to the divertor plates and the first wall. The plasma flow to the divertor plates, Φ_d, is calculated by $\Phi_d = 4\pi R\theta \int_0^{Lr} \Gamma_d(r)dr$, where $r = \rho a$, R, a, and L_r denote the major, minor radii and an effective distance between the separatrix and the first wall, respectively. The plasma flow to the first wall, Φ_w, is calculated by $\Phi_w = (D_\perp n_{iSOL}/\lambda_n)\exp(-L_r/\lambda_n)S_{sep}$ where S_{sep} is the area of the separatrix surface. A part of neutrals produced at the divertor plates, $\eta_r \Phi_d$, are reionized in the divertor region. The global divertor recycling coefficient η_r is recalculated from the flux-tube value in the five-point model as $\eta_r = 1 - \Gamma_d(0)\lambda_n(1 - \exp(-L_r/\lambda_n))(1 - \eta'_r)/(\int_0^{Lr} \Gamma_d(r)dr)$. The remained part of neutrals produced at the divertor plates is pumped out from the divertor ($\Phi_{dpump} = f_{dpump}\Phi_d$) or escapes from the divertor region to the radial direction ($\Phi_{nr} = f_{dr}\Phi_d$) or to the divertor throat ($\Phi_{nth} = (1 - f_{dpump} - f_{dr} - \eta_r)\Phi_d$). Then, these fractions Φ_{nr} and Φ_{nth} go to the core region. Neutrals produced at the first wall (Φ_w) escape from the SOL to the core region. Neutrals are also added by gas puffing in the core region (Φ_{puf}).

3. Integrated simulation result

The ELM activity is simulated for JT-60U like parameters: $R = 3.4$ m, $a = 0.9$ m, $\kappa = 1.5$, $\delta = 0.26$, $I_p = 1.5$ MA, $B_t = 3.5$ T and $q_{95} = 4.5$. The ELM parameters are chosen as $\tau_{ELM} = 200$ μs, $\chi_{ELM}^{max} = 100$ m²/s and $\Delta_{ped} = 0.05$ on ρ. The values of τ_{ELM} and Δ_{ped} are typical values in experiments [1,14]. On the other hand, the value of χ_{ELM}^{max} is chosen to obtain ELM energy and particle losses comparable with JT-60U experiments [14]. The other parameters are chosen as $\Phi_{puf} = 0.3 \times 10^{22}$ s^{-1}, $f_{dpump} = 0.01$, $f_{dr} = 0.02$, $L_r = 0.4$ m and $T_n = 3$ eV.

Figure 1 shows the time evolution of (a) the electron part of the stored energy, W_{se}, the ion part, W_{si}, the total stored energy, W_s, (b) the volume averaged electron density, $<n_e>$, (c) Q_r, (d) Γ_{re}, (e) T_{SOL}, T_{div}, (f) n_{eSOL} and n_{ediv}. The simulation starts at nearly stationary state and the reduction of diffusivities for the pedestal begins at $t = 0.03$ s. Along the pedestal growth, the temperature and density increase in the pedestal region and the stored energies and the averaged density increase in Fig.1(a) and (b). The ion SOL temperature is higher than the electron one, while the divertor plasma temperatures is lower than the SOL ones due to the

high recycling divertor plasma. In the progress of the pedestal growth, ELMs occur from $t =$ 0.2 s where medium-n modes (n = 8-11) become unstable. Figure 2 shows profiles of the electron temperature and density just before and after each ELM crash. A typical profile of the ELM enhanced diffusivity is shown in Fig.7(b) (narrower one). The ion temperature at the pedestal top, T_{iped} ~ 2 keV, is higher than the electron one T_{eped} ~ 1.3 keV at the ELM onset. The collapse and the formation of pedestal profiles repeats and those profiles are almost the same in the ELMs. Thus, the energy loss is almost constant in each ELM crash.
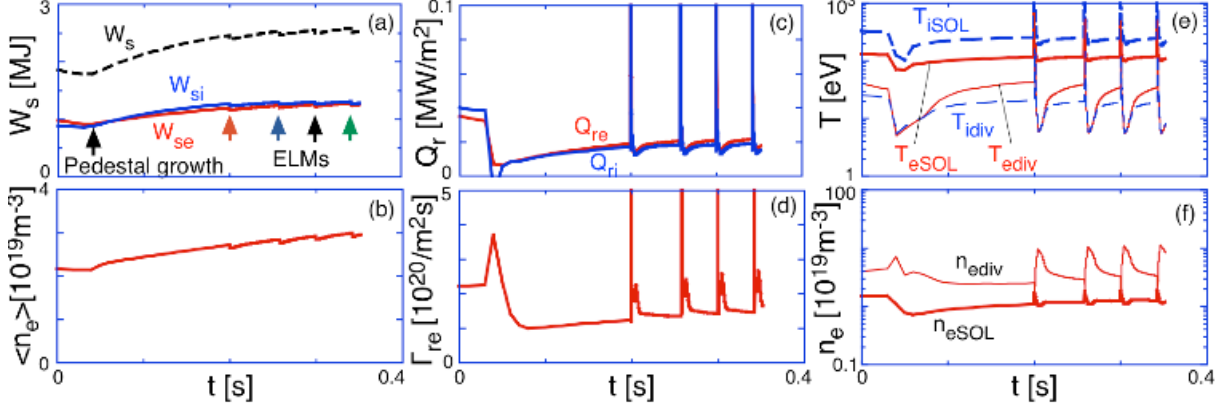
Fig. 1 Time evolution of (a) W_{se}, W_{si}, W_s, (b) $<n_e>$, (c) Q_{re}, Q_{ri}, (d) Γ_{re}, (e) T_{eSOL}, T_{ediv}, T_{iSOL}, T_{idiv} (f) n_{eSOL} and n_{ediv}. Profiles at each ELM are shown in Fig.2.

We consider the power balance in the ELM cycle. The power balance is approximately described by an equation, $W_s' \equiv dW_s/dt \approx P_{heat} - P_{tr} - P_{CX}$, where P_{heat} is the heating power, P_{tr} and P_{CX} are loss powers by the transport and the charge-exchange (CX). Figure 3 shows the time evolution of W_s, P_{tr} and P_{CX} of the previous simulation in Fig.1. There are two periods; one is the ELM phase where the energy, ΔW_{ELM}, is lost by P_{trELM} and P_{CXELM} and the other is the inter-ELM phase where the heating recovers the stored energy depending on the loss powers, P_{trint} and P_{CXint}. The time-averaged equation is given by $\overline{P_{in}} \equiv \overline{P_{heat}} - \overline{W_s'} \approx \overline{P_{trint}} + \overline{P_{CXint}} + \overline{P_{ELM}}$ where $\overline{P_{in}}$ is the net heating power and $\overline{W_s'}$ is evaluated by a broken line in Fig.3. The ELM loss power, $\overline{P_{ELM}}$, is defined by $\overline{P_{ELM}} = f_{ELM} \Delta W_{ELM}$ where f_{ELM} is the ELM frequency. For example, in the previous simulation, the power balance is kept as $\overline{P_{in}} = 8.7$ MW, $\overline{P_{trint}} = 5.4$ MW, $\overline{P_{CXint}} = 1.6$ MW and $\overline{P_{ELM}} = 1.7$ MW.

4. Power dependence of ELM energy loss and cycle

We study the power dependence of the ELM energy loss and cycle. Figure 4(a) shows the time evolution of W_s for three values of the net heating power. The collapse of pedestal profiles is almost the same among the different input powers, while the core stored energy increases with the input power. The ELM energy loss is almost constant in present conditions, $\Delta W_{ELM} \approx 67$ kJ. Additionally, loss powers by the inter-ELM transport
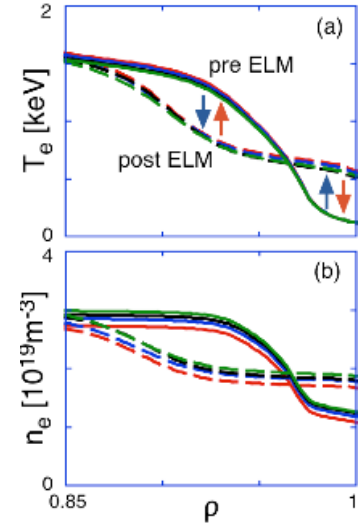

Fig.2 Profiles of T_e and n_e just before and after each ELM crash in Fig.1.
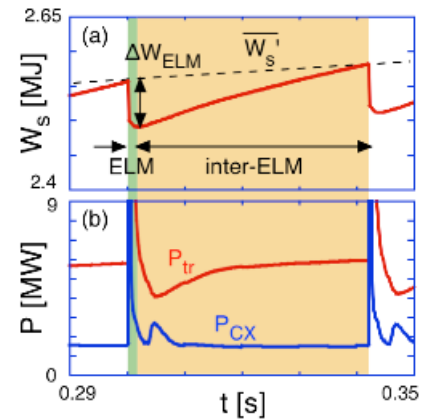

Fig.3 Time evolution of (a) W_s, (b) P_{tr} and P_{CX} between ELMs for a simulation of Fig.1.

and the CX are almost constant, $\overline{P_{\text{trint}}} \approx 5.4$ MW and $\overline{P_{\text{CXint}}} \approx 2.0$ MW. Figure 4(b) shows the ELM frequency as a function of the net input power. Simulation results almost correspond to a line given by an analytical formula, $f_{\text{ELM}} = (\overline{P_{\text{in}}} - \overline{P_{\text{trint}}} - \overline{P_{\text{CXint}}})/\Delta W_{\text{ELM}}$. Thus, the ELM frequency linearly increases with the input power, as was observed in experiments [15].
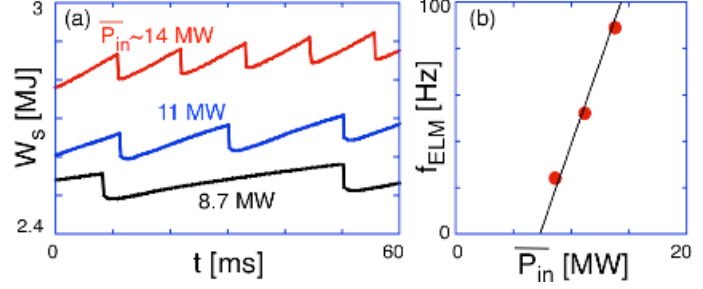

Fig.4 (a) Time evolution of W_s for $\overline{P_{in}}$=8.7, 11 and 14 MW. (b) f_{ELM} versus $\overline{P_{in}}$.

5. Collisionality dependence of ELM energy loss and cycle

The effect of the pedestal collisionality is investigated. The pedestal density and temperature are varied by the gas puffing with $\Phi_{\text{puf}} = 0.3\text{-}2\times10^{22}$ s^{-1}. Thus, the normalized electron collisionality of the pedestal plasma, $v^*_{\text{ped}} = \pi R q_{95}/\lambda_{\text{ee}}$ where λ_{ee} is the electron mean free path, increases from 0.095 to 0.72. In the following ELMs after the first ELM, the ELM energy loss varies and saturates a certain value. Figure 5 shows the dependence of the saturated ΔW_{ELM}, its electron component, ΔW_{e}, and ion one, ΔW_{i}, normalized by the pedestal energy, W_{ped}, on v^*_{ped} where the case with the lowest v^*_{ped} corresponds to that in Fig.1. The

Fig.5 Dependence of ΔW_{ELM}, ΔW_e and ΔW_i normalized by W_{ped} on v^*_{ped}.

saturated ELM energy loss deviates a little from that at the first ELM in [13], but the collisionality dependence is almost the same. Thus, the cause of the collisionality dependence is the same as found in [13]. The bootstrap current and SOL transport cause the dependence of the electron conductive energy loss. On the other hand, the electron convective energy loss is almost constant in the v^* variation because the ELM particle loss is independent of the collisionality as the same as found in experiments [1]. For lower collisionality, the ion temperature becomes higher than the electron one due to the ineffectiveness of the equipartition proportional to the collisionality. As a result, ion convective and CX losses bring the collisionality dependence of the ion energy loss. The reduction of the total energy loss becomes comparable with that in experiments [1].
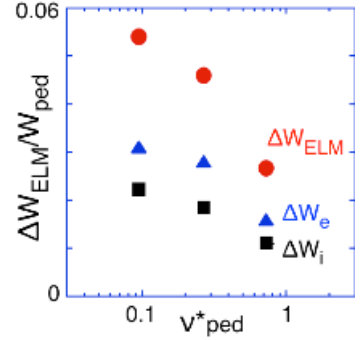
In the present simulation, there are three loss power channels, $\overline{P_{\text{trint}}}$, $\overline{P_{\text{CXint}}}$ and $\overline{P_{\text{ELM}}}$. Figure 6(a) shows the loss power ratio as a function of the collisionality where the collisionality is varied by the gas puffing in cases A-C. As the collisionality decreases, the inter-ELM transport is reduced and the ELM loss power is enhanced, as found in experiments [3]. Figure 6(b) shows the ELM energy loss against the ELM frequency in the same cases. For almost constant inter-ELM transport in the high collisionality, the cases B and C, the large ELM energy loss reduces the ELM frequency by extending the time to recover the pedestal profile to its pre-ELM state. As a result, the loss power due to ELMs keeps almost constant, as was observed in experiments [4]. Thus, the ELM energy loss and the inter-ELM transport determine the ELM cycle.

Here, we define the normalized energy confinement time between ELMs, $\tau_E^{\text{int}*}$, by $\tau_E^{\text{int}*} \equiv \tau_E^{\text{int}}/\tau_B$, where $\tau_E^{\text{int}} = \overline{W_s}/\overline{P_{\text{trint}}}$, $\tau_B = a^2/\chi_B$ and the Bohm diffusivity $\chi_B = T_{\text{eped}}/16eB$. In the JT-60U experimental analysis [4], a scaling of $\tau_E^{\text{int}*}$ was found as $\tau_{\text{scal}}^* = 0.234(v^*_{\text{ped}})^{-0.6}(\rho^*_{\text{pol}})^{-0.7}$, where ρ^*_{pol} is the normalized poloidal gyro radius of the pedestal plasma. Figure 6(c) shows

the comparison of simulation results and the scaling where parameter ranges are $0.067 < v^*_{ped}$ < 0.72 and $0.020 < \rho^*_{pol} < 0.037$. The ρ^*_{pol} range is 0.020-0.029 in Fig.6(a) and thus the data with different values of I_p and B_t and so on is added in Fig.6(c). The inter-ELM energy confinement time agrees well with the JT-60U scaling.
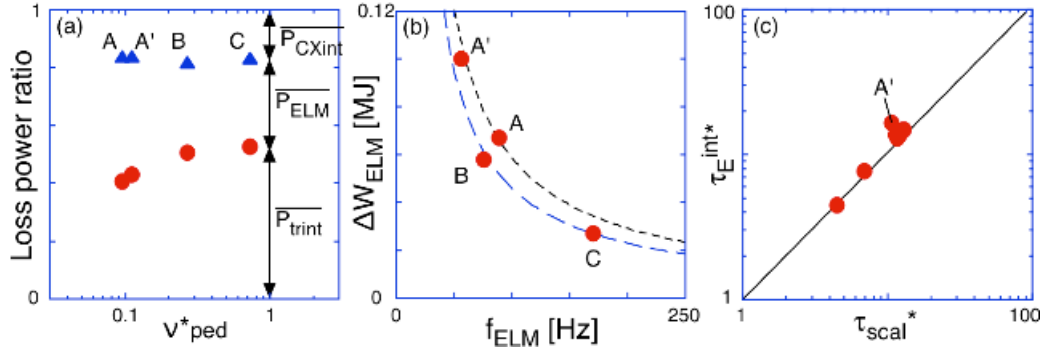

Fig.6 (a) Dependence of $\overline{P_{trint}}$, $\overline{P_{ELM}}$, and $\overline{P_{CXint}}$ normalized by $\overline{P_{in}}$ on v^*_{ped} where $\overline{P_{in}}$=14-15 MW. (b) ΔW_{ELM} versus f_{ELM}. (c) τ_E^{int*} versus τ_{scal}^*. In (a) and (b), collisionality is varied by gas puffing in cases A-C and pressure gradient inside pedestal is steepened in case A'. In (b), dashed and dotted lines mean $\overline{P_{ELM}}$ =4.6 and 5.8 MW, respectively.

6. Dependence of ELM energy loss and cycle on the pressure gradient inside the pedestal

The effect of the pressure gradient inside the pedestal top on the ELMs is investigated. The steep pressure gradient inside the pedestal top is one of the major features for improved H-mode plasmas. Figure 7(a) shows two profiles of the total pressure, p, just before each ELM crash where $\overline{P_{in}}$~14 MW and the transport is reduced in a region of $0.8<\rho<0.925$ inside the pedestal top at ρ=0.925 in the case with higher pressure. The pressure gradient inside the pedestal top is different, while the pedestal profile is almost the same and thus v^*_{ped}~0.1 in both cases. Even the pressure gradient inside the pedestal top in the case with lower pressure is a little larger than those observed in JT-60U [14,16]. The H_{H98y2} factor increases from 0.97 to 1.3 in Fig.7(a). The steep pressure gradient inside the pedestal top broadens the eigenfunctions of unstable modes and thus the region of the ELM enhanced transport in Fig.7(b). The detailed dependence of the MHD mode structure on the pressure profile inside the pedestal was studied by using the MARG2D [17].

Fig.7 Profiles of (a) p just before each ELM and (b) χ_{ELM} during the first instability for different pressure gradients inside pedestal top at ρ=0.925.

Figure 8 shows the time evolution of W_s for the two cases with p'_{in}/p'_{ped}= 0.14 and 0.53 in Fig.7 where p'_{in} and p'_{ped} denote $dp/d\rho$ inside and at the pedestal, respectively. In the case with p'_{in}/p'_{ped}=0.14, medium-n modes produce the same energy loss in each ELM and the ELM cycle is regular as already shown in the previous sections. On the other hand, in the case with p'_{in}/p'_{ped}=0.53, subsequent instabilities arise. Figure 9 shows the time evolution of the pressure profile in an ELM at t~25 ms in Fig.8. A collapse makes regions with the steep pressure gradient, which causes the next instability. While the first instability is caused by medium-n modes (n~10), the subsequent ones are caused by higher-n modes (n>20), i.e., the infinite-n mode is unstable. In Fig.7, the subsequent instabilities move inward and thus do not
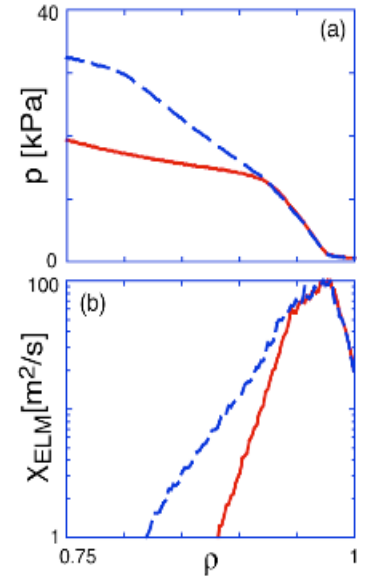
much enhance the energy loss because the transport remains low near the separatrix at ρ=1. When a subsequent instability arises near the separatrix, the energy loss is enhanced as shown in an ELM at t~43 ms in Fig.8. The large amount of energy transported from the inside region induces the subsequent instability near the separatrix. As a result, in the case with the steep pressure gradient, the ELM energy loss varies and the ELM cycle becomes irregular sometimes. Figure 10 shows the normalized ELM energy loss $\Delta W_{ELM}/W_{ped}$ as a function of p'_{inped}/p'_{ped}, where an open circle represents a value obtained by taking account of only the first instability. The minimum value of the energy loss (closed circle with lower value), in which the subsequent instabilities arise far from the separatrix, is a little larger than those obtained by taking account of only the first instability (open circle). The dependence of the minimum energy loss on p'_{in}/p'_{ped} is almost the same as found in [12], in which only the first instability was taken into account and the density was not yet solved. As shown in Fig.10, the steep pressure gradient inside the pedestal top enhances the ELM energy loss by both the extension of the ELM enhanced transport in the first instability and the subsequent instability near the separatrix.

As shown in Fig.6(a) (A for p'_{in}/p'_{ped}=0.14 and A' for p'_{in}/p'_{ped}=0.53), the inter-ELM transport is almost the same between the two cases in Fig.8. In the case with p'_{in}/p'_{ped}=0.53,

the ELM frequency is evaluated by using continuous ELMs with the same energy loss (for example, t~6 and 25 ms in Fig.8, lower loss in Fig.10). The evaluated ELM frequency is plotted as a function of the ELM energy loss in Fig.6(b). The large ELM energy loss reduces the ELM frequency so that the power loss due to ELMs keeps almost constant. The inter-ELM energy confinement time is also evaluated and plotted in Fig.6(c). The value of the inter-ELM energy confinement time with p'_{in}/p'_{ped}=0.53 almost agrees with, but deviates a little from the JT-60U scaling compared with the other data with p'_{in}/p'_{ped}~0.1. This may relate with the low pressure gradient inside the pedestal in JT-60U experiments [14,16].

Fig.8 Time evolution of W_s for p'_{in}/p'_{ped}=0.14 and 0.53 in Fig.7.

Fig.9 Time evolution of (a) p and (b) χ_{ELM} profiles in an ELM with p'_{in}/p'_{ped}=0.53 at t~25 ms in Fig.8 where lines denote 0.2 ms interval (solid →dashed→dotted→ chain).

Fig.10 $\Delta W_{ELM}/W_{ped}$ as a function of p'_{in}/p'_{ped} for ν^*_{ped}~0.1 where an open circle denotes a value obtained by taking account of only the first instability.

7. Conclusion

The ELM energy loss and cycle have been studied by using the TOPICS-IB. The TOPICS-IB reproduces a series of ELMs with the following characteristics. The ELM energy loss increases with decreasing the collisionality and the ELM frequency increases linearly with the
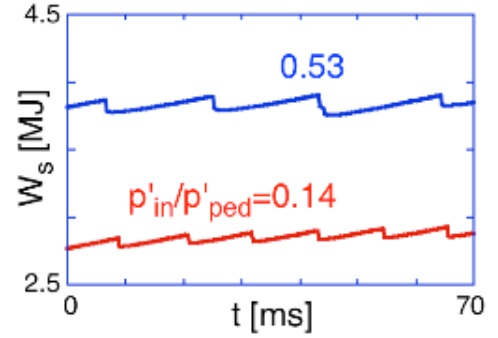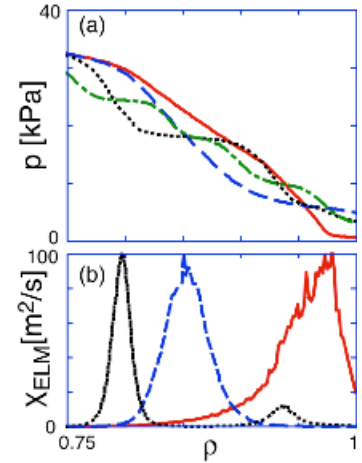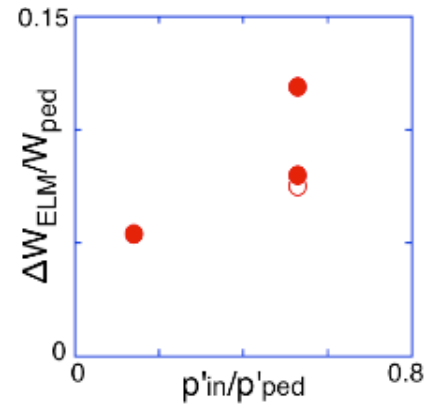
input power, as the same as experiments of type-I ELMs. The transport model with the pedestal neoclassical transport connected to the SOL parallel transport reproduces the inter-ELM transport, which decreases in the low collsionality so that the ELM loss power is enhanced as observed in experiments. The inter-ELM energy confinement time agrees with the scaling based on the JT-60U data. The steep pressure gradient inside the pedestal top, required for improved H-mode plasmas with the H_{H98y2} factor above unity, is found to enhance the ELM energy loss and reduce the ELM frequency so that the ELM loss power remains constant. The steep pressure gradient inside the pedestal top broadens the region of the ELM enhanced transport and induces subsequent instabilities. When the large energy is transported near to the separatrix by the instabilities, a subsequent instability arises near the separatrix and makes an additional loss.

In order to validate our models, the further comparison with experiments and nonlinear simulations are future works. The model improvement, such as the transport model which determines the pressure gradient inside the pedestal top, the pedestal width, and so on, is necessary. Key physics of the JT-60U scaling of the inter-ELM energy confinement will be examined by artificially modifying the simulation model. The experimental analysis of the effect of the steep pressure gradient inside the pedestal top on the ELMs is underway.

References

[1] LOARTE, A., et al., Plasma Phys. Control. Fusion **45** (2003) 1549.
[2] LEONARD, A.W., et al., J. Nucl. Mater. **313-316** (2003) 768.
[3] URANO, H., et al., J. Plasma Fusion Res. **81** (2005) 280.
[4] URANO, H., et al., Phys. Rev. Lett. **95** (2005) 035003.
[5] ONJUN, T., et al., Phys. Plasmas **12** (2005) 012506.
[6] LONNROTH, J.S., et al., Contrib. Plasma Phys. **46** (2006) 726.
[7] PANKIN, A.Y., et al., Nucl. Fusion **46** (2006) 403.
[8] WIESEN, S., et al., Contrib. Plasma Phys. **48** (2008) 201.
[9] HAYASHI, N., et al., Nucl. Fusion **47** (2007) 682.
[10] HAYASHI, N., et al., J. Nucl. Mater. **363-365** (2007) 1044.
[11] AIBA, N., et al., Nucl. Fusion **47** (2007) 297.
[12] HAYASHI, N., et al., Contrib. Plasma Phys. **48** (2008) 196.
[13] HAYASHI, N., et al., J. Phys. Conf. Series **123** (2008) 012025.
[14] OYAMA, N., et al., Nucl. Fusion **44** (2004) 582.
[15] KAMADA, Y., et al., Plasma Phys. Control. Fusion **36** (1994) A123.
[16] SHIRAI, H., et al., Plasma Phys. Control. Fusion **42** (2000) 1193.
[17] AIBA, N., et al., J. Phys. Conf. Series **123** (2008) 012008.